Journal Pre-proof

Enhancing fully printable mesoscopic perovskite solar cell performance using integrated metallic grids to improve carbon electrode conductivity

Dimitrios Raptis, Vasil Stoichkov, Simone Meroni, Adam Pockett, Carys Worsley, Matthew Carnie, Dave Worsley, Trystan Watson
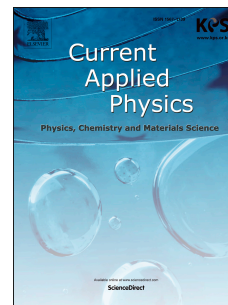
Please cite this article as: D. Raptis, V. Stoichkov, S. Meroni, A. Pockett, C. Worsley, M. Carnie, D. Worsley, T. Watson, Enhancing fully printable mesoscopic perovskite solar cell performance using integrated metallic grids to improve carbon electrode conductivity, *Current Applied Physics* (2020), doi: https://doi.org/10.1016/j.cap.2020.02.009.

This is a PDF file of an article that has undergone enhancements after acceptance, such as the addition of a cover page and metadata, and formatting for readability, but it is not yet the definitive version of record. This version will undergo additional copyediting, typesetting and review before it is published in its final form, but we are providing this version to give early visibility of the article. Please note that, during the production process, errors may be discovered which could affect the content, and all legal disclaimers that apply to the journal pertain.

Enhancing fully printable mesoscopic perovskite solar cell performance using integrated metallic grids to improve carbon electrode conductivity

Dimitrios Raptis, Vasil Stoichkov, Simone Meroni, Adam Pockett, Carys Worsley, Matthew Carnie, Dave Worsley, Trystan Watson*

SPECIFIC – Swansea University, Materials Research Centre, College of Engineering, Bay Campus, Swansea, SA1 8EN, United Kingdom

Abstract

Carbon based Perovskite Solar cells (C-PSCs) have emerged as the most promising candidates for commercialisation in the field of perovskite photovoltaics, as they are highly stable, low cost and make use of easily scaled manufacturing techniques. However, the limited conductivity of the carbon electrode inhibits performance and represents a significant barrier to commercial application. This work presents a scalable method for enhancing the carbon electrode conductivity through the integration of aluminium and copper grids into prefabricated C-PSCs. Adhered to the cells using an additional low temperature carbon ink, the metallic grids were found to dramatically reduce top electrode series resistance, leading to a large improvement in fill factor and efficiency. After grid integration, the 1 cm^2 C-PSCs yielded power conversion efficiency (PCE) of 13.4% and 13% for copper and aluminium respectively, while standard C-PSCs obtained PCE of 11.3%. Performance is also significantly augmented in the case of larger-scale 11.7 cm^2 modules, where PCEs went from 7.7% to 10% and 11% for aluminium and copper grids respectively. This technique offers a fast and low temperature route to high-performance, large-area C-PSCs and could therefore have serious potential for application to the high-volume manufacture of perovskite cells and modules.

Keywords

Metallic grid; Highly conductive carbon electrode; Low temperature carbon ink; Carbon based perovskite solar cell; Module; Enhanced efficiency

1. Introduction

Organic-inorganic lead halide perovskite solar cells (PSCs) have made rapid progress in recent years, with power conversion efficiency (PCE) improvements from 3.8% to 23.7% since 2009 [1-7]. However, a range of issues must still be overcome in order to produce commercially viable devices. The high cost of materials such as organic hole transporters [8], the stability of devices in operation, and issues related to upscaling all represent significant barriers to commercialisation [9].

Mei *et al.* in 2014 presented a fully printable, hole transporter-free device, that consisted of sequentially applied layers of TiO$_2$, ZrO$_2$ and carbon applied to FTO glass [10]. The perovskite solution is deposited by liquid infiltration through the stack [11, 12] and subsequent drying. TiO$_2$ acts as electron transporter from the perovskite to the FTO electrode while ZrO$_2$ acts as an insulating spacer and the conductive carbon as the top electrode. This device structure is shown schematically in Fig. 1a.

These devices, so-called Carbon based Perovskite Solar Cells (C-PSCs), overcome the stability issues observed in many other perovskite architectures. For example, high stability of 10,000 h under continuous 1 sun illumination has been reported for C-PSC with the 2D/3D 5-ammonium valeric acid (NH$_3$(CH$_2$)4COOH$^+$,5-AVA) perovskite [13]. This stability evidence combined with the industrially applicable screen-printing processes that are used has identified this device structure as a potential front-runner to the market [14]. Large area modules have already been demonstrated with PCE between 10 and 11% on 10 x 10 cm^2 [15-17] and around 6% PCE for A4 sized modules [18].

In terms of efficiency, lab scale cells lag behind other types of PSCs. The record for triple mesoporous C-PSCs stands at 15.9% for a methylammonium lead iodide (MAPI) perovskite, chemically modified by adding SrCl$_2$ [19]. One of the main reasons for the limited C-PSCs performance is the low conductivity of the carbon electrode compared to conventional evaporated metal electrodes [20]. Although several other cathode materials including Au [21, 22] and Ni [23] have been explored, carbon materials remain the most promising as they are cheap, printable, stable and inherently water resistant. Improving the carbon electrode conductivity is therefore key to achieving the PCE improvements required for commercially competitive performance.

The potential benefits of using metallic grids to improve the conductivity of a transparent conductive electrode has been previously discussed by Meredith *et al* [20]. In this work, we show that the use of copper and aluminium grids can also lead to highly conductive top electrodes for use in C-PSCs. For the placement of the metallic grids on the top contact, we use a home-made, low temperature carbon ink that acts as a conductive binder (Fig. 1b). We chose this structure over thin foils as the grid design allows for conducting ink permeation, and thus coverage on both sides of the metal, firmly adhering it on the cell without destroying the carbon layer (Fig. 1c). We also avoided a vacuum evaporation process because of its high energy consumption [24].

The conventional C-PSC, shown in Fig. 1a, requires a porous carbon electrode in order to facilitate infiltration of the perovskite ink; following drying this layer is responsible for charge extraction and conductivity. The direct application of the metallic grids to this existing layer would create an even thicker scaffold whereby infiltration and penetration of the subsequent perovskite liquid ink would be impossible. Furthermore, there would be no adhesion between the grid and the underlying layer leading to instant delamination. To resolve this, the C-PSC devices were infiltrated prior to the application of the grid electrode and the grid itself combined with a separate carbon conducting ink acting as a binder. This sequence can be seen in Fig. 1.

The standard carbon paste formulation used for the top contact in the original device structure typically requires heating at 400°C in order to achieve the porosity necessary for enabling perovskite infiltration and for overall conductivity. This formulation therefore is inappropriate as a subsequent additional electrode due to these temperature requirements degrading the underlying perovskite [25, 26]. Hence, the use of it as conducting glue for the post-infiltration grids placement is unsuitable. A low temperature carbon ink was therefore developed for this purpose.

The effect of grid placement on device performance is examined for 1 cm^2 cells before application to larger modules of series-interconnected cells. Standard C-PSCs are used as reference samples and C-PSCs with the additional carbon ink, in the absence of grid, are also examined for comparison (Fig. 1a, b and c). It is revealed that the metallic grid integration significantly enhances device performance in both 1cm^2 and upscaled devices. These improvements are a consequence of drastically improved fill factors, due to the enhanced electrode conductivity. This simple, low temperature method offers an

easy route to improve device performance and therefore has serious potential for application in the high-volume manufacture of large-area perovskite devices.

2. Experimental

2.1 Materials

PbI$_2$ (99%, Sigma-Aldrich), MAI (CH$_3$NH$_3$I, anhydrous, Dyesol), 5-ammonium valeric acid iodide (5-AVAI, Dyesol) and γ-Butyrolactone (Sigma Aldrich) were used as received for preparation of perovskite precursors. Stacks were prepared using the following: anhydrous 2-propanol (IPA, 99.5%), carbon paste (Gwent electronic materials), ZrO$_2$ paste (Solaronix), TiO$_2$ paste (30NR-D, Dyesol), terpineol (95%, Sigma-Aldrich), and titanium diisopropoxide bis(acetylacetonate) (TAA, 75% in IPA, Sigma-Aldrich). The materials for the additional home-made carbon ink are as follows: Graphite Timrex SFG 15 (Imerys), Carbon black Ensaco 250G (Imerys), Ethyl Cellulose (Sigma-Aldrich), 1-Butanol (Sigma-Aldrich). Conductive fluorine-doped tin oxide glass (FTO, TEC7, XOP) was used as the substrate. Aluminium and copper grids (25 μm thick) were provided by Dexmet.

2.2 Device fabrication

For 1cm^2 devices FTO substrates were patterned with a Nb:YVO4 laser (532 nm) before cleaning with a solution of ~2 % Hellmanex in deionised water, rinsing with acetone and IPA and a 5 minute plasma clean in O$_2$. A compact TiO$_2$ (cTiO$_2$) blocking layer was then deposited at 300°C by spray pyrolysis of 10% titanium diisopropoxide bis(acetylacetonate) in IPA. Next, the mesoporous TiO$_2$ paste was diluted 1:1 by weight in terpineol before screen printing and subsequent sintering at 550 ^{o}C. The mesoporous ZrO$_2$, and carbon were then screen printed and annealed at 400 ^{o}C. Room temperature perovskite precursor solution (14 μlcm^2, made using 0.439 gcm^{-3} PbI$_2$, 0.1514 gcm^{-3} MAI and 0.0067 gcm^{-3} 5-AVAI in γ-Butyrolactone) was then drop cast onto the cooled stack. Devices were left in air for ten minutes to allow the solution to percolate through the stack before annealing in a fan oven for 1 h at 50 ^{o}C. The finished cells were then exposed to a standard 70% relative humidity process at 40 °C for 24 hours to induce a recrystallisation [27] and then dried in a vacuum oven before measuring.

Module substrates (5 cm^2) were laser etched with lines every 6.5 mm before cTiO$_2$ and mesoporous layer depositions as described above. The annealed layers were then mechanically scribed 0.3 mm away from the etched lines to define the contact area width (0.4 mm). The carbon layer was then printed and annealed as outlined above before a final scribing step every 5.2 mm to separate the cells. Perovskite was deposited using the automated infiltration method described in previous work [11] and annealed for 1 hour at 50 ^{o}C in an extraction oven.

Electrodes used for conductivity measurements were printed on clean glass and annealed at 400 ^{o}C. Standard samples were tested as produced. Ink samples were prepared by coating standard electrodes with the additional homemade, low temperature ink and drying at 60 ^{o}C for 5 minutes in air. Metal grids were applied as described below.

2.3 Ink Fabrication, Grid Application and Encapsulation

The additional low temperature ink consisted of a polymeric binder and a mix of carbon allotropes. Ethyl Cellulose was chosen as the polymeric binder due to its high solubility, low toxicity and low cost. The ink prepared contained 12.5% Ethyl Cellulose resin in 1g 1-Butanol and had 29.4% carbon loading.

Grids are placed directly onto the carbon electrode and the additional ink is applied on-top. Due to the porous nature of the grids, the ink travels through the pores allowing coverage of both sides. The grid is then firmly placed on top of the mesoporous carbon layer and dried at 60°C for 5 minutes in air. The thickness of the additional ink was controlled by using polyimide tape around the cell active area. By this way, a stable and reproducible carbon electrode with integrated metallic grid was produced (Fig. 1c).

Devices for stability testing were encapsulated using commercially available two-part epoxy resin and a glass back cover (Fig. 1d).
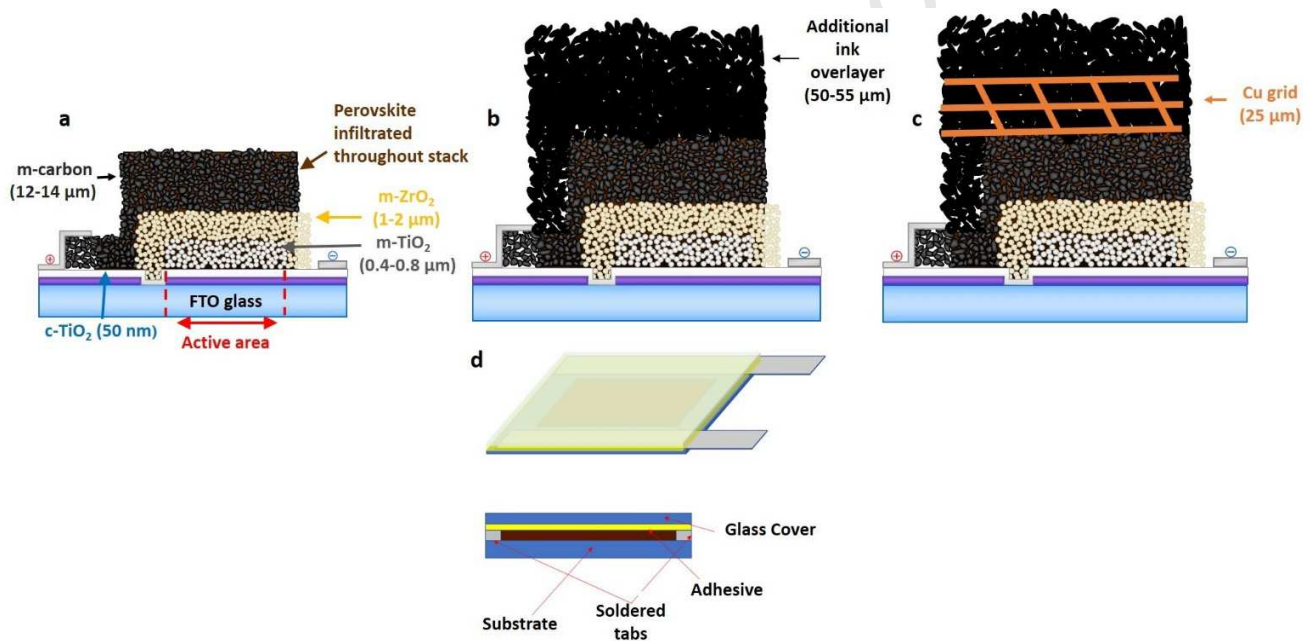
Fig. 1. Schematic representation of (a) standard C-PSC (b) + Additional ink overlayer (c) + Additional ink overlayer containing Cu grid and (d) encapsulation mechanism used.

In the case of larger upscaled devices, a mask made by polyimide, was used to protect the inter-connect areas from shorting during grid integration. After the placement of polyimide at junctions, the ink/grid application on the active areas of the module is completed as described above (Fig. 2).
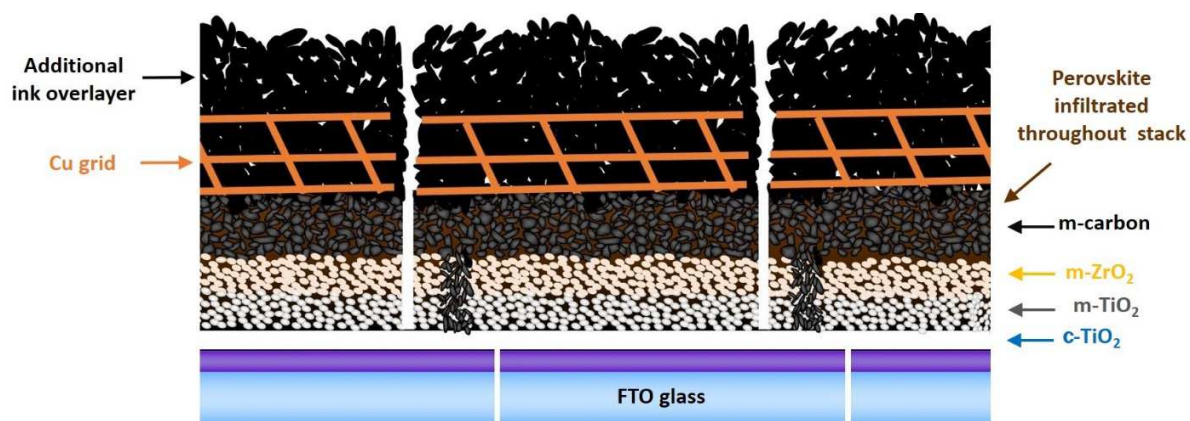
Fig. 2. Schematic representation of a module with copper grid. Layers thicknesses are the same as Fig.1.

2.4 Characterization techniques

All IV testing was performed under a class AAA solar simulator (Newport Oriel Sol3A) at AM1.5 100 mW cm^{-2} illumination, calibrated using a KG5 filtered reference cell. Cell area was masked to 0.49 cm^2 for 1 cm^2 devices, while modules were not masked. Devices were light soaked for 3 minutes before current density (J) – voltage (V) sweeps were performed from open-circuit voltage (V$_{OC}$) to short-circuit current density (J$_{SC}$) and vice versa at a rate of 330 mV/s using a Keithley 2400 source meter. Stability measurements were performed at 1 sun illumination using a Solaronix Solixon A-20 AM1.5G AAA solar simulator. Cells were placed on a cooled platform to maintain a temperature of ~21 ^{o}C and scanned once every hour using a Keithley 2400 source meter.

Sheet resistances were measured using a JANDEL RM 3000 Four-Point Probe System. Electrochemical impedance spectroscopy (EIS) measurements were performed on unmasked devices using a Zahner CIMPS-X photoelectrochemical workstation. Devices were scanned from 10MHz to 1 Hz at open circuit under red LED illumination (630nm) at 1 sun equivalent intensity. Electrode topography was examined using a HITACHI scanning electron microscope (SEM), while films thicknesses (Fig. 1) were measured with a DEKTAK 150 profilometer system.

3. Results and discussion

Aiming to attain a high conductive top electrode for hole-transporter-free carbon perovskite solar cells, aluminium and copper grids were placed on-top of the standard carbon electrode by using an additional homemade carbon ink as glue. Initial tests compared the conductivity of four different electrodes: the standard carbon electrode (std), standard carbon electrode plus additional ink overlayer (+ink), standard carbon electrode plus additional ink overlayer containing copper grid (+Cu) and standard carbon electrode plus additional ink overlayer containing aluminium grid (+Al). Fig. 3a shows the sheet resistance of the different electrodes. The standard carbon electrode produces 22.5 Ω/□ sheet resistance on a glass substrate while the electrode with additional carbon ink produces 13.6 Ω/□ sheet resistance. When metallic grids are also applied, this value is drastically decreased. The aluminium grid lead to less than 1 Ω/□ sheet resistance while the copper produces an electrode with almost metallic (0.005 Ω/□) electrical resistance.

5

Typically, increasing the electrode thickness can cause a reduction in measured sheet resistance and so this should be considered when comparing values. This is accounted for in Fig. 3b where electrode thickness is accounted for by multiplying the measured resistivity with the corresponding electrode thickness. The measured decrease in resistance remains significant for both electrodes containing metal grids, even when accounting for the large increase in thickness. This is not the case for the additional ink coated samples, in the absence of grids, where the observed conductivity improvement is clearly a consequence of the thicker layer.
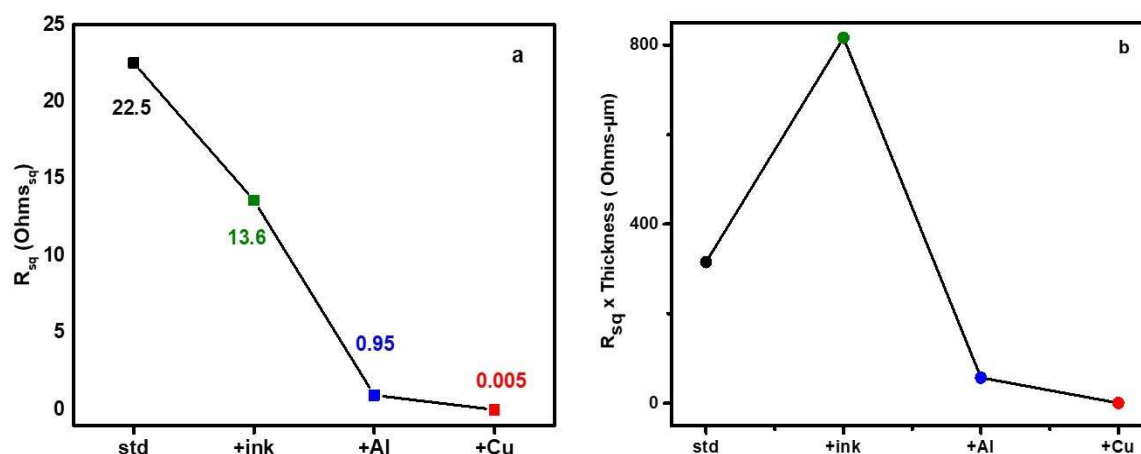
Fig. 3. (a) Sheet resistance of different carbon electrodes (b) Sheet resistance multiplied with sample thickness of different electrodes.

Device performances were measured before and after grid application, with multiple devices measured in order to ascertain that observed differences were not a consequence of in-batch variability. The statistical results are presented, before and after enhancement, in Fig. 4 and the average values in Table 1. In all cases metallic grid placement vastly improves device performance: Average PCE increased from 11.19 ± 0.27% to 13.15 ± 0.12% with copper grid application and from 11.08 ± 0.14% to 12.83 ± 0.06% with aluminium. These improvements are mainly due to a >10 % increase in fill factor (FF). A small improvement in J_{sc} was also observed in the case of copper grids, which explains the higher increase in device PCE. A smaller enhancement in average PCE from 11.32 ± 0.06% to 11.80 ± 0.13%, was observed in the case of additional ink on top of the cells without any metallic grid.

6
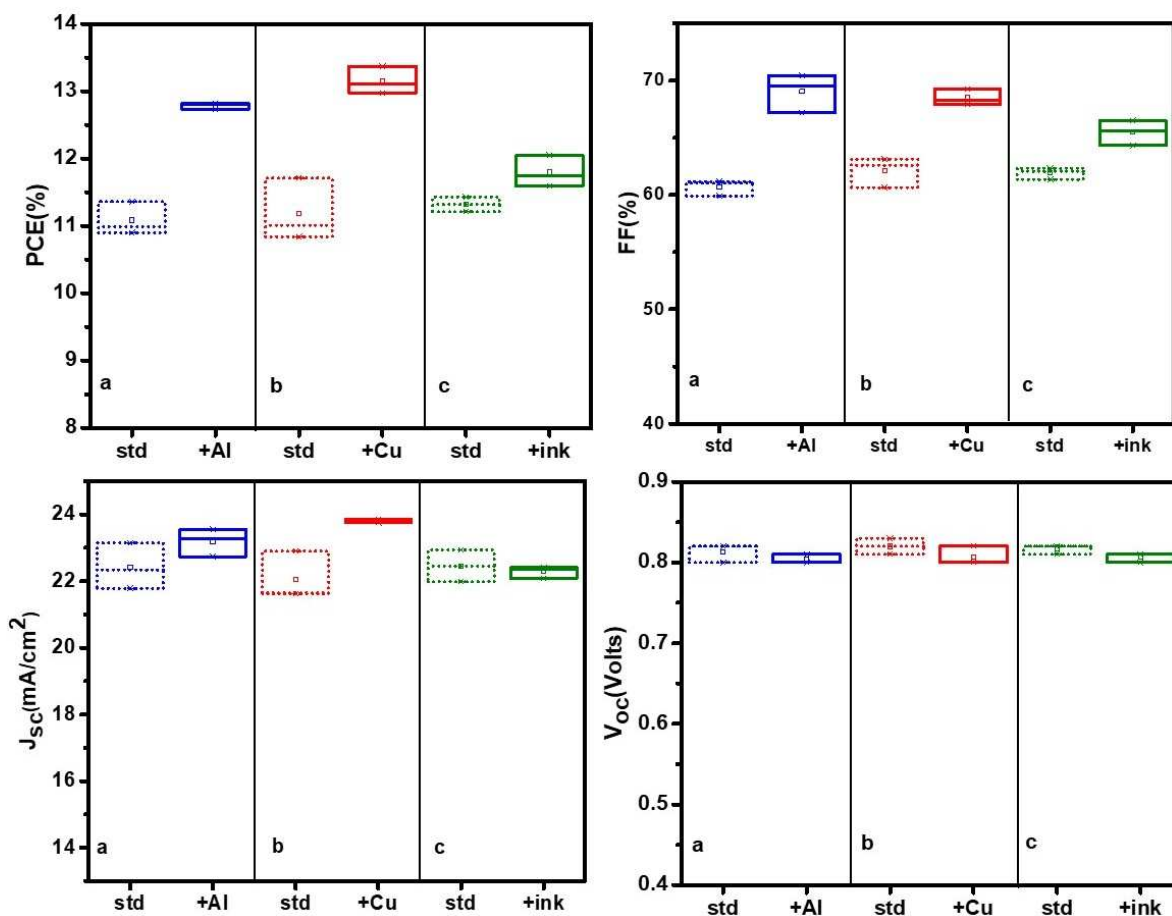
Fig. 4. Box plots of main photovoltaic parameters of several C-PSCs. (a) before and after the placement of aluminium grid (b) before and after the placement of copper grid (c) before and after the placement of additional carbon ink. Data comprises an average of 3 devices per case.

Top Electrode	PCE (%)	FF (%)	V_{oc} (Volts)	J_{sc} (mA/cm^2)
Std	11.08 ± 0.14	60.70 ± 0.40	0.81 ± 0.01	22.42 ± 0.40
+Al	12.83 ± 0.06	69.04 ± 0.97	0.80 ± 0.01	23.19 ± 0.24
Std	11.19 ± 0.27	62.12 ± 0.75	0.82 ± 0.01	22.06 ± 0.42
+Cu	13.15 ± 0.12	68.48 ± 0.40	0.81 ± 0.01	23.79 ± 0.03
Std	11.32 ± 0.06	61.92 ± 0.29	0.82 ± 0.01	22.46 ± 0.28
+ink	11.80 ± 0.13	65.48 ± 0.64	0.81 ± 0.01	22.29 ± 0.10

Table 1. Average performance of cells with different carbon electrodes.

The J-V curves for the highest performing devices are shown in Fig. 5a with detailed photovoltaic parameters listed in Table 2. The champion devices exhibit PCEs of 12.95%, 13.37% and 12.05% for

aluminium, copper and additional ink-only electrodes respectively. The largest improvement was observed with copper, which showed an increase in device performance of 23.3%, while the aluminium showed an increase of 18.81%. Addition of ink alone results in a modest improvement of 6.45%. Series resistance values calculated from the J-V curves of the cells are also presented in Table 2. A reduction of R_s is evident after grid application for both aluminium and copper and is responsible for the enhanced performance of our devices.

The above results can be easily rationalised using the conductivity data (Fig. 3). Fill factor is determined by competition between charge extraction and recombination. A more conductive electrode results in enhanced charge extraction and therefore improved fill factor, which in turn increases the PCE. Although addition of the homemade carbon ink was also found to decrease Rs values this was to a much lesser degree, consistent with the difference in measured conductivity.

It is well known that the use of standard characterization techniques can easily lead to inaccurate experimental efficiency [28]. Previous reports on mesoscopic hole transporter-free carbon cells have accounted for this problem by measuring devices at their maximum power point to obtain the stabilised power output [29, 30]. Peak power tracking was therefore performed on devices before and after top electrode modifications. The corresponding graphs from the champion devices are presented in Fig. 5b. The standard cells used for grid testing exhibited similar stabilized PCEs before grid placement, 9.62% for aluminium samples and 9.77% for copper. These values increased to 11.50% (+Al) and 11.87% (+Cu) after grid application, while the performance of the additional ink-only cells improved by a smaller degree (9.85% for standard samples, 10.42% for samples with ink). These values both support the original J-V data and verify that observed improvements in device performance are a direct consequence of grid application.
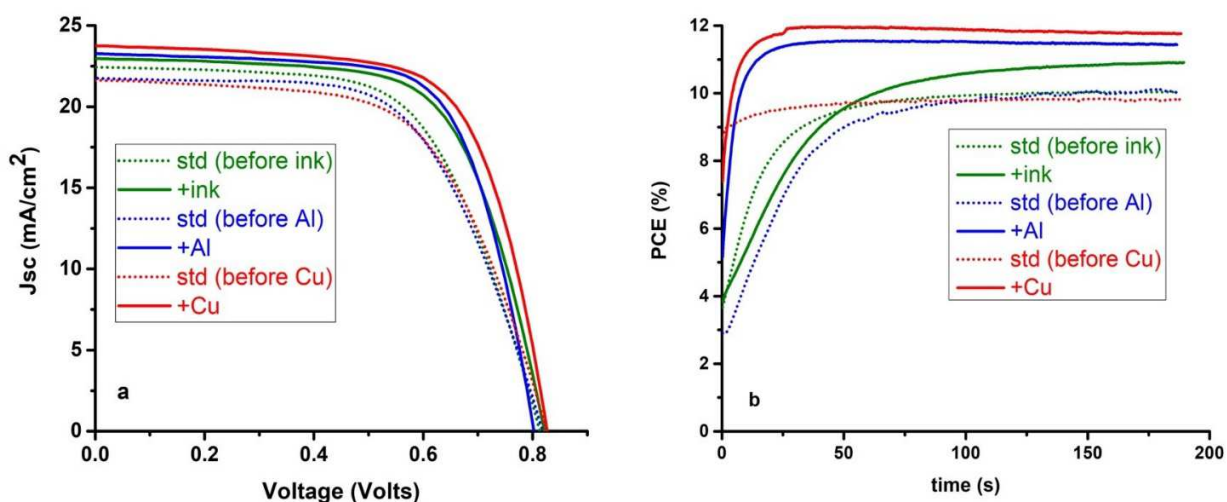
Fig.5. (a) J-V curves of the champion devices before and after the placement of grids/ink (b) Stabilised PCE at one sun of champion devices before and after the placement of the relevant grids and ink.

Top Electrode	PCE (%)	FF (%)	V_{oc} (Volts)	J_{sc} (mA/cm^2)	R_s (Ωcm^2)
std	10.90	61.17	0.82	21.78	8.73
+Al (champion)	12.95	69.54	0.80	23.27	4.86
std	10.84	60.65	0.83	21.65	8.42
+Cu (champion)	13.37	68.26	0.82	23.75	4.85
std	11.32	62.08	0.81	22.45	7.92
+ink (champion)	12.05	66.50	0.81	22.37	5.96

Table 2. Photovoltaic parameters of champion solar cells before and after ink and grid application.

Once the positive effect of grid inclusion on electrode conductivity and device performance had been confirmed, the impact of the metal grids was further analysed using impedance spectroscopy. In Fig. 6a we present an equivalent circuit for the carbon devices, where $R_{S,1}$ and $R_{S,2}$ are the resistances associated with the FTO and carbon (with or without metallic grid) respectively. R_P and C represent the combination of resistances and capacitances that contribute to the impedance response of the active layer of the device [31, 32]. For example, R_P, is the total resistance arising from the parallel combination of the recombination resistance, and shunt resistance due to pinholes. Similarly, C is the total capacitance due to the geometric capacitance of the device, and charge accumulation (chemical capacitance) in the active layer. As $R_{S,1}$ and $R_{S,2}$ are electrically indistinguishable they can be combined to give R_S, as shown in the further simplified equivalent circuit in Fig. 6b, along with the expected impedance response of such a circuit. At high frequency, the impedance of the capacitive elements tends to zero – the capacitor therefore represents a short-circuit to current flow, and so the overall impedance response is governed by R_S. The effect of the metal grids on the resistance of the carbon layer can therefore be interpreted by analysing the high frequency intercept of the impedance response with the x-axis of a Nyquist plot, which gives the value of R_S.

The impedance response of the carbon cells with different top electrode configurations is shown in Fig. 6c. It can be seen that the impedance response is not simply a single semi-circular arc as given by our equivalent circuit. The analysis of the electronic and ionic processes occurring in the active layer of these devices is beyond the scope of this work [30], and the equivalent circuit given here is simply used to demonstrate that the properties of the carbon layer can be interpreted from the value of R_S. The extracted values of R_S for each of the cathode configuration devices are shown in the inset table in Fig. 6c. The inclusion of metallic grids leads to a four-fold decrease in the value of R_S relative to the standard device – a smaller decrease than that, observed for the additional ink alone. This shows that the effective resistance of the carbon contact has been decreased, which is consistent with the improvement in fill factor observed above in the J-V measurements (Fig. 3, 4). The difference between the two metallic grids can not be resolved as they are both highly conductive, with the remaining resistance of 2.1 Ω cm^2 for both the aluminium and copper grid devices likely dominated by the resistance of the FTO contact. It should be noted that R_S in the equivalent circuit does not relate to the

9

series resistance as defined by the J-V measurements – the 'dc' or low frequency limit of the impedance response relates to the slope of the J-V curve near open-circuit.
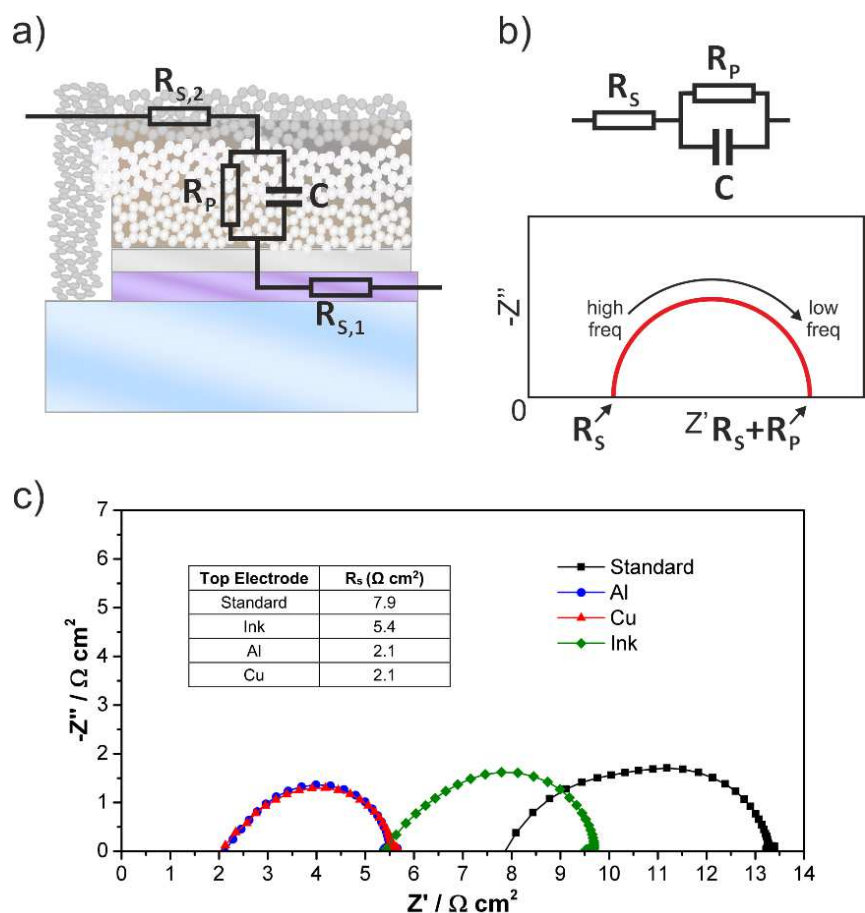
Fig. 6. (a) Equivalent circuit of carbon cell. $R_{S,1}$ is FTO resistance, $R_{S,2}$ is carbon resistance and R_PC represents active layer effective resistance and capacitance (b) Simplified equivalent circuit and expected impedance response (Nyquist plot). R_S is the sum of the FTO and carbon resistances (c) Impedance response of carbon devices with different top electrode configurations. Inset table shows the Rs values, calculated from impedance response for each of the different top electrode configuration devices

Scanning electron microscope (SEM) was performed to show the morphology of the grids in-situ and the extent of additional ink coverage. Fig. 7a and b present the surface SEM images, including Energy-dispersive X-ray spectroscopy (EDX) analysis, of the cells with the integrated copper and aluminium grid respectively. It is clear that the additional ink permeate the mesh structure and is present on both sides of the grid, which accounts for the mechanical stability of the layer.
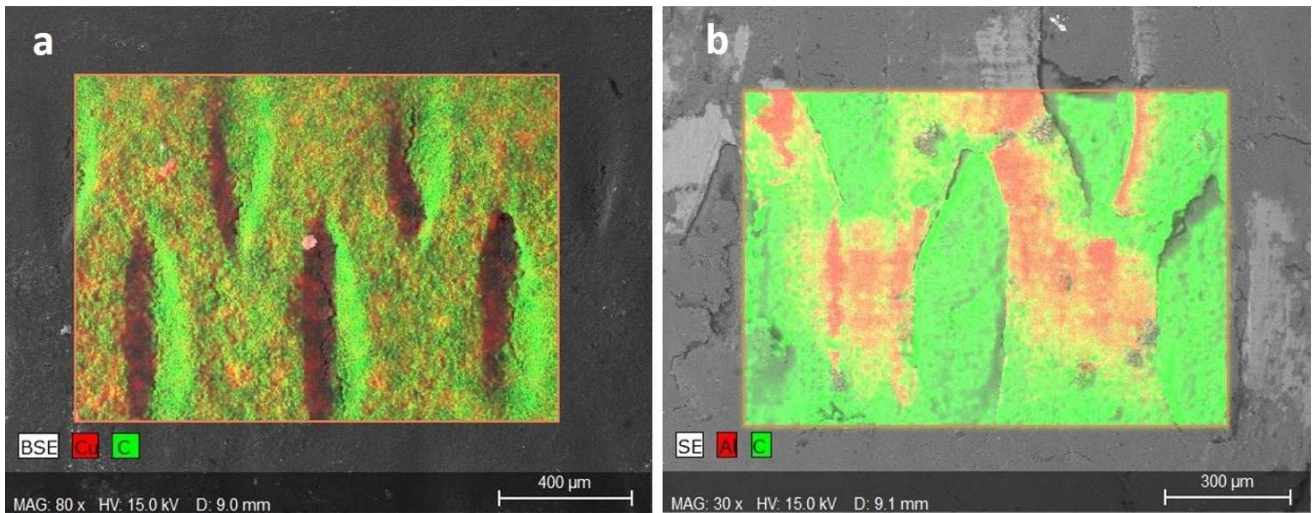
Fig. 7. Surface SEM images, including EDX analysis, of devices with (a) copper and (b) aluminium grid.

Long term stability of the cells with grid addition was tested under continuous illumination after encapsulation. Standard cells were used as a reference sample. The time evolution of normalized device PCEs over 700 hours is displayed in Fig. 8. Compared to standard cell, both grid samples exhibit slightly improved stability. This fact indicates that the additional carbon ink not only helps the grids to adhere on top of the cell but also may provide an additional protection to the device. Therefore,
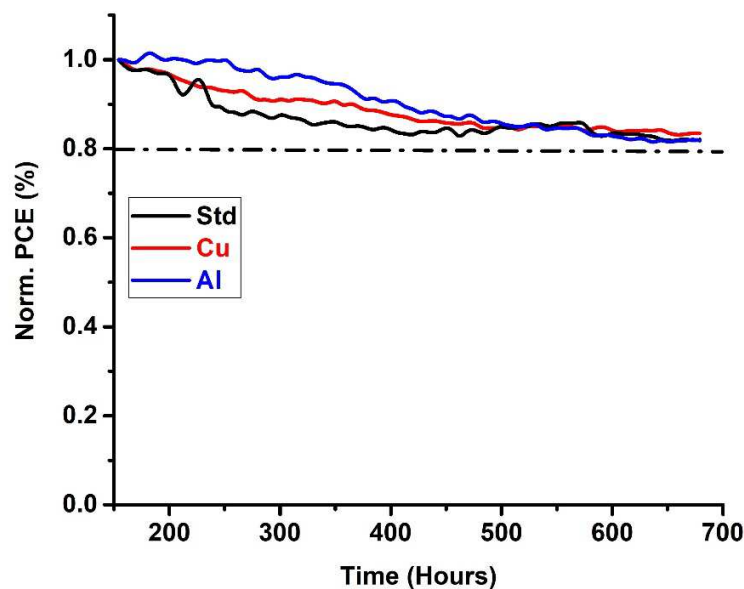
metals do not negatively affect device lifetime.

Fig. 8. Normalised PCE values showing the long term stability of C-PSCs with different cathode electrodes.

The above results demonstrate the positive effect of metallic grid application on 1cm^2 solar cells. As previously stated, these device architectures are considered one of the most commercially applicable

11

and have been used to produce large scale modules. The negative impact of the highly resistive carbon electrode is known to be more detrimental to performance as device area increases [15, 33]. Consequently, the effect of grid application on module performance was examined, as well. Upscaling devices are constructed by 6 interconnected cells with total active area, 11.7 cm^2, as shown schematically in Fig. 2. The relevant current-voltage (IV) characteristics are shown in Fig. 9a, while the corresponding photovoltaic parameters are summarized in Table 3. A significant reduction of R_s values, calculated from IV curves, can be observed in all devices after grid placement. The introduction of copper has as a result a high improvement of fill factor from 43.44% to 59.18% which in turn increases the PCE from 7.70% to 11.05%. The introduction of aluminium achieves enhanced performance on another device, as well. The fill factor of the standard module before the aluminium application was 46.68% with an efficiency at 7.73%, increasing to 56.77% and 9.97% respectively post-application.

For a more accurate reading of device efficiency and to confirm the PCE enhancements observed from J-V data, peak power tracking measurements were performed (Fig. 9b). The stabilised efficiencies of the standard devices are 7.02% and 7.03%, improving to 9.88% and 8.86% for copper and aluminium
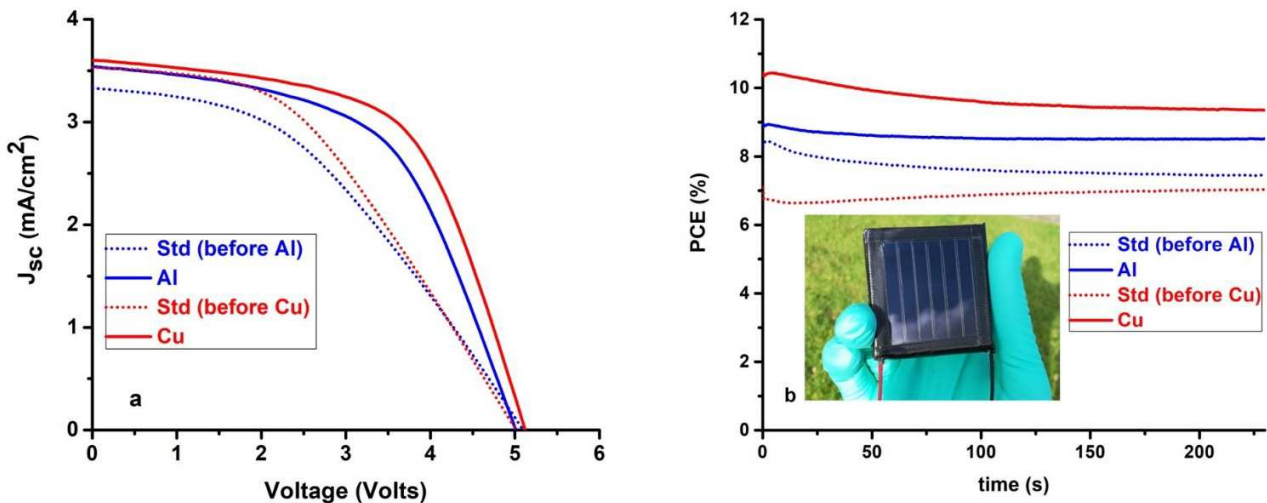
respectively after grid application.

Fig. 9. (a) J-V curves of the 11.7 cm^2 modules before and after grid application (b) Stabilised PCEs of modules before and after the placement of metallic grids. Inset shows the photo of a 11.7 cm^2 module

Cathode Electrode of modules	PCE (%)	FF (%)	V_{oc} (Volts)	Average V_{oc} per cell (Volts)	I_{sc} (mA)	Minimum I_{sc} per cell (mA)	J_{sc} (mA/cm^2)	Rs (Ohms)
Std	7.73	46.68	4.95	0.83	39.20	20.10	3.35	56.68
Al	9.97	56.77	5.03	0.84	41.84	21.45	3.49	35.85
Std	7.70	43.44	5.02	0.84	41.35	21.21	3.53	64.87
Cu	11.05	59.18	5.11	0.85	42.73	21.91	3.65	29.99

Table 3. Photovoltaic parameters of modules before and after application of different carbon electrodes.

Module improvements compare to those observed at small scale samples are much higher because, placing the metallic grid on the active area of each cell decreases the series resistance and therefore improves the fill factor of every separate cell. Consequently, the whole device records much higher overall fill factor and efficiency. This fact may pave the way for an industrial module with high conductive top electrode. Despite similar standard device performance before grid placement, the application of copper grids led to greater performance enhancement than aluminium in all trialled devices. This is likely a consequence of the higher conductivity of the produced electrode (Fig. 3). It should be noted that the measured performance enhancements are significant in both cases with both materials offering substantial improvements in efficiency.

4. CONCLUSION

A simple technique is presented for enhancing C-PSCs PCE through the application of low resistance top electrodes. The high resistance of the carbon electrode in C-PSCs limits device performance by negatively impacting on the fill factor and represents a significant barrier to commercialisation. This work shows that integration of copper and aluminium grids onto the carbon layer of pre-fabricated devices using low-temperature carbon ink drastically improves the performance of both small and upscaled devices. This is particularly notable in the case of copper, where grid application to a $1cm^2$ device resulted in a champion PCE of 13.37%, a 23.3% improvement compared to the standard cell. Efficiencies were also improved with aluminium grids, where measured PCE reached 12.95%, up from 10.90% pre-application. The slightly lower impact of aluminium was found to be a consequence of lower electrode conductivity.

This method is perhaps most applicable to large scale modules, where high resistance electrodes are more detrimental to device performance. When grids applied to 11.7 cm^2 modules, PCEs improved from 7.70% to 11.05% for copper and 7.73% to 9.97% for aluminium. Again, fill factor was significantly enhanced (36.23% and 21.62% for copper and aluminium respectively).

The development of cheap and simple methods for improving baseline performance is essential for commercialisation. This technique offers a simple, ambient, low temperature route to drastically improve device performance without adversely affecting stability. Combined with improving the TCO conductivity, this method would allow the production of high efficiency devices and modules, and therefore represents a simple potential route to the production of commercially competitive C-PSCs.

References

[1] A. Kojima, K. Teshima, Y. Shirai, T. Miyasaka, Organometal halide perovskites as visible-light sensitizers for photovoltaic cells, J. Am. Chem. Soc. 131 (2009) 6050-6051. https://doi.org/10.1021/ja809598r.

[2] M.M. Lee, J. Teuscher, T. Miyasaka, T.N. Murakami, H.J. Snaith, Efficient hybrid solar cells based on meso-superstructured organometal halide perovskites, Science 338 (2012) 643-647. 10.1126/science.1228604.

[3] W. S. Yang, J. H. Noh, N. J. Jeon, Y. C. Kim, S. Ryu, J. Seo, S. I. Seok, High-performance photovoltaic perovskite layers fabricated through intramolecular exchange, Science 348 (2015) 1234-1237. https://doi.org/10.1126/science.aaa9272.

[4] D. Zhao, Y. Yu, C. Wang, W. Liao, N. Shrestha, C. R. Grice, A. J. Climaroli, L. Guan, R. J. Ellingson, K. Zhu, X. Zhao, R. Xiong, Y. Yan, Low-bandgap mixed tin–lead iodide perovskite absorbers with long carrier lifetimes for all-perovskite tandem solar cells, Nat. Energy 2 (2017) 17018. https://doi.org/10.1038/nenergy.2017.18.

[5] W. S. Yang, B. W. Park, E. H. Jung, N. J. Jeon, Y. C. Kim, D. U. Lee, S. S. Shin, J. Seo, E. K. Kim, J. H. Noh, S. I. Seok, Iodide management in formamidinium-lead-halide-based perovskite layers for efficient solar cells, Science 356 (2017) 1376-1379. 10.1126/science.aan2301.

[6] Best Research-Cell efficiency chart, Photovoltaic Research, NREL, https://www.nrel.gov/pv/cell-efficiency.html, (accessed 25 October 2019).

[7] H. J. Snaith, Present status and future prospects of perovskite photovoltaics, Nat. Mater. 17 (2018) 372 -376. https://doi.org/10.1038/s41563-018-0071-z.

[8] M. Zhang, M. Lyu, H. Yu, J.-Ho Yun and Q. Wang, L. Wang, Stable and low-cost mesoscopic $CH_3NH_3PbI_2Br$ perovskite solar cells by using a thin poly(3-hexylthiophene) layer as a hole transporter, Chem. Eur. J. 21 (2015) 434–439. https://doi.org/10.1002/chem.201404427.

[9] J. A. Baker, Y. Mouhamad, K. Hooper, D. Burkitt, M. Geoghegan, T. M. Watson, From spin coating to roll-to-roll: investigating the challenge of upscaling lead halide perovskite solar cells, IET Renew Power Gener. 11 (2017) 546–549. https://doi.org/10.1049/iet-rpg.2016.0683.

[10] A. Mei, X. Li, L. Liu, Z. Ku, T. Liu, Y. Rong, M. Xu, M. Hu, J. Chen, Y. Yang, M. Grätzel, H. Han, A hole-conductor free, fully printable mesoscopic perovskite solar cell with high stability. Science 345 (2014) 295–298. 10.1126/science.1254763.

[11] S. M. P. Meroni, Y. Mouhamad, F. De Rossi, A. Pockett, J. Baker, R. Escalante, J. Searle, M. J. Carnie, E. Jewell, G. Oskam, T. M. Watson, Homogeneous and highly controlled deposition of low viscosity inks and application on fully printable perovskite solar cells, Sci. Technol. Adv. Mater. 19 (2018) 1–9. https://doi.org/10.1080/14686996.2017.1406777.

[12] Z. Ku, Y. Rong, M. Xu M, T. Liu, H. Han, Full printable processed mesoscopic $CH_3NH_3PbI_2/TiO_2$ heterojunction solar cells with carbon counter electrode, Sci Rep. 3 (2013) 3132. https://dx.doi.org/10.1038%2Fsrep03132.

[13] G. Grancini, C. R. Carmona C, I. Zimmermann I, E. Mosconi, X. Lee, D. Martineau, S. Narbey, F. Oswald, F. De Angelis, M. Graetzel, M. K. Nazeeruddin, One-Year stable perovskite solar cells by 2D/3D interface engineering, Nat. Commun. 8 (2017) 15684. 10.1038/ncomms15684.

[14] H. Chen H, S. Yang, Carbon-based perovskite solar cells without hole transport materials: the front runner to the market?, Adv. Mater. 29 (2017) 1603994. https://doi.org/10.1002/adma.201603994 .

[15] A. Priyadarshi, L. J. Haur, P. Murray, D. Fu, S. Kulkarni, G. Xing, T. C. Sum, N. Mathews, S. G. Mhaisalkar, A large area (70 cm^2) monolithic perovskite solar module with a high efficiency and stability, Energy Environ. Sci. 9 (2016) 3687–3692. 10.1039/c6ee02693a.

[16] A. Bashir, S. Shukla, J. H. Lew, S. Shukla, A. Bruno, D. Gupta, T. Baikie, R. Patidar, Z. Akhter, A. Priyadarshi, N. Mathews, S. G. Mhaisalkar, Spinel Co_3O_4 nanomaterials for efficient and stable large area carbon-based printed perovskite solar cells, Nanoscale 10 (2018) 2341–2350. 10.1039/c7nr08289d.

[17] Y. Hu, S. Si, A. Mei, Y. Rong, H. Liu, X. Li, H. Han, Stable Large-Area ($10 \times 10\ cm^2$) Printable Mesoscopic Perovskite Module Exceeding 10% Efficiency, Sol. RRL, 1 (2017) 1600019. https://doi.org/10.1002/solr.201600019.

[18] F. De Rossi, J. A. Baker, D. Beynon, K. E. A. Hooper, S. M. P. Meroni, D. Williams, Z. Wei, A. Yasin, C. Charbonneau, E. H. Jewell, T. M. Watson, All Printable Perovskite Solar Modules with 198 cm^2 Active Area and Over 6% Efficiency, Adv. Mater. Technol. 3 (2018) 1800156. https://doi.org/10.1002/admt.201800156.

[19] H. Zhang, H. Wang, S. T. Williams, D. Xiong, W. Zhang, C. C. Chueh, W. Chen, A. K. Y. Jen, $SrCl_2$ Derived Perovskite Facilitating a High Efficiency of 16% in Hole-Conductor-Free Fully Printable Mesoscopic Perovskite Solar Cells, Adv. Mater. 29 (2017). 10.1002/adma.201606608.

[20] P. Meredith, A. Armin, Scaling of next generation solution processed organic and perovskite solar cells, Nat. Commun. 9 (2018) 5261. https://doi.org/10.1038/s41467-018-05514-9.

[21] L. Etgar, P. Gao, Z. Xue, Q. Peng, A. K. Chandiran, B. Liu, M. K. Nazeeruddin, M. Gratzel, Mesoscopic $CH_3NH_3PbI_3/TiO_2$ Heterojunction Solar Cells, J. Am. Chem. Soc. 134 (2012) 17396. https://doi.org/10.1021/ja307789s.

[22] W. A. Laban, L. Etgar, Depleted hole conductor-free lead halide iodide heterojunction solar cells, Energy Environ. Sci. 6 (2013) 3249. 10.1039/C3EE42282H.

[23] Z. Ku, X. Xia, H. Shen, N. H. Tiep, H. J. Fan, A mesoporous nickel counter electrode for printable and reusable perovskite solar cells, Nanoscale, 7 (2015) 13363. 10.1039/C5NR03610K.

[24] B. E. Hardin, H. J. Snaith, M. D. McGehee, The renaissance of dye-sensitized solar cells, Nat. Photon. 6 (2012) 162–169. https://doi.org/10.1038/nphoton.2012.22.

[25] F. C. Krebs. Fabrication and processing of polymer solar cells: a review of printing and coating techniques, Sol. Energ. Mat. Sol. Cells. 93 (2009) 394–412. 10.1016/j.solmat.2008.10.004.

[26] J. A. Baker, D. Deganello D, D. T. Gethin, T. W. Watson, Flexographic printing of graphene nanoplatelet ink to replace platinum as counter electrode catalyst in flexible dye sensitised solar cell, Mater. Res. Innov. 18 (2014) 86– 90. https://doi.org/10.1179/1433075X14Y.0000000203.

[27] J. Troughton, K. Hooper, T. M. Watson, Humidity resistant fabrication of $CH_3NH_3PbI_3$ perovskite solar cells and modules, Nano Energy. 39 (2017) 60-68. 10.1016/j.nanoen.2017.06.039.

[28] R. B. Dunbar , B. C. Duck , T. Moriarty , K. F. Anderson , N. W. Duffy , C. J. Fell , J. Kim , A. Ho-Baillie , D. Vak , T. Duong , Y. Wu , K. Weber , A. Pascoe , Y.-B. Cheng , Q. Lin , P. L. Burn , R. Bhattacharjee , H. Wang , G. J. Wilson, How reliable are efficiency measurements of perovskite solar cells? The first inter-comparison, between two accredited and eight non-accredited laboratories, J. Mater. Chem. A, 5 (2017) 22542 -22558. 10.1039/C7TA05609E.

[29] H. L. Hsu, C. C. Chang, C. P. Chen, B. H. Jiang, R. J. Jeng, C. H. Cheng, High-performance and high-durability perovskite photovoltaic devices prepared using ethylammonium iodide as an additive, J. Mater. Chem. A 3 (2015) 9271 -9277. 10.1039/C5TA01563D.

[30] L. Wagner, S. Chacko, G. Mathiazhagan, S. Mastroianni, A. Hinsch, High Photovoltage of 1 V on a Steady-State Certified Hole Transport Layer-Free Perovskite Solar Cell by a Molten-Salt Approach, ACS Energy Lett. 3 (2018) 1122 -1127. https://doi.org/10.1021/acsenergylett.8b00293.

[31] A. Pockett, G. E. Eperon, T. Peltola, H. J. Snaith, A. Walker, L. Peter, P. J. Cameron, Characterization of Planar Lead Halide Perovskite Solar Cells by Impedance Spectroscopy, Open-Circuit Photovoltage Decay, and Intensity-Modulated Photovoltage/Photocurrent Spectroscopy, J. Phys. Chem. C 119 (2015) 3456-3465. https://doi.org/10.1021/jp510837q.

[32] A. Pockett, G. E. Eperon, N. Sakai, H. J. Snaith, L. Peter, P. J. Cameron, Microseconds, Milliseconds and Seconds: Deconvoluting the Dynamic Behaviour of Planar Perovskite Solar Cells, Phys. Chem. Chem. Phys. 19 (2017) 5959-5970. 10.1039/C6CP08424A.

[33] Y. Mouhamad, S. M. P. Meroni, F. De Rossi, J. Baker, T. M. Watson, J. Searle, E. H. Jewel, Geometrical optimization for high efficiency carbon perovskite modules, Sol. Energy 187 (2019) 129-136. https://doi.org/10.1016/j.solener.2019.05.047.

17

Highlights

- A simple and scalable method for attaining a highly conductive carbon electrode through the integration of metallic grids into prefabricated C-PSCs.

- A low temperature carbon ink was developed to act as conducting glue for grid placement.

- The champion PCE of 1 cm^2 C-PSCs is boosted from 11.3% to 13.4% by copper grid integration.

- When grids applied to 11.7 cm^2 modules, PCEs improved from 7.7% to 10 % and 11 % for aluminium and copper grids respectively.

Declaration of interests

☒ The authors declare that they have no known competing financial interests or personal relationships that could have appeared to influence the work reported in this paper.

☐The authors declare the following financial interests/personal relationships which may be considered as potential competing interests: